research papers

30-Lens interferometer for high-energy X-rays

Mikhail Lyubomirskiy,[a] Irina Snigireva,[a]* Victor Kohn,[b] Sergey Kuznetsov,[c] Vyacheslav Yunkin,[c] Gavin Vaughan[a] and Anatoly Snigirev[d]

[a]ESRF, Grenoble 38043, France, [b]National Research Centre 'Kurchatov Institute', Moscow 123182, Russian Federation, [c]Institute of Microelectronics Technology RAS, Chernogolovka 142432, Russian Federation, and [d]Baltic Federal University, Kaliningrad 236041, Russian Federation. *Correspondence e-mail: irina@esrf.fr

A novel high-energy multi-lens interferometer consisting of 30 arrays of planar compound refractive lenses is reported. Under coherent illumination each lens array creates a diffraction-limited secondary source. Overlapping such coherent beams produces an interference pattern demonstrating strong longitudinal functional dependence. The proposed multi-lens interferometer was tested experimentally at the 100 m-long ID11 ESRF beamline in the X-ray energy range from 30 to 65 keV. The interference pattern generated by the interferometer was recorded at fundamental and fractional Talbot distances. An effective source size (FWHM) of the order of 15 μm was determined from the first Talbot image, proving the concept that the multi-lens interferometer can be used as a high-resolution tool for beam diagnostics.

1. Introduction

The advent of the brilliant highly coherent X-ray beams produced by third-generation synchrotrons and free-electron lasers has triggered the development of coherent optics and interferometry. Introduced almost 20 years ago (Snigirev *et al.*, 1996), compound refractive lenses (CRLs) offer a number of practical advantages compared with other micro- and nano-optics, as they are easy to align, stable and relatively insensitive to misorientations and mechanical vibrations, and coherence-preserving (Snigirev & Snigireva, 2008). Thus, the use of refractive optics has quickly expanded and they are now in common use on various beamlines at 15 synchrotrons in ten countries. This development was intensified after the successful implementation of transfocators with a variable number of lenses offering focal length and energy tunability (Snigirev *et al.*, 2009a; Vaughan *et al.*, 2011). CRLs can be easily adapted to very high X-ray energies by modifying the composition of the lens material and number of lenses. CRLs are widely employed for micro- and nanobeam focusing, microscopy, beam conditioning, monochromatization, harmonic rejection (Lengeler *et al.*, 1999a,b; Drakopoulos *et al.*, 2002; Vaughan *et al.*, 2011; Polikarpov *et al.*, 2014), and other applications. Using the intrinsic property of the refractive lens as a Fourier transformer, coherent diffraction microscopy and high-resolution diffraction methods have been proposed (Drakopoulos *et al.*, 2005; Petukhov *et al.*, 2006; Bosak *et al.*, 2010; Ershov *et al.*, 2013). The significant progress in Si microfabrication technology has allowed the manufacturing of Si planar refractive lenses for nanofocusing (Schroer *et al.*, 2003; Aristov *et al.*, 2000). This has led to a completely new direction of development of refractive optics, namely in-line X-ray interferometry. A bi-lens interferometer, which under coherent illumination generates an interference

field with a variable period ranging from tens of nanometres to tens of micrometres, was proposed and tested (Snigirev *et al.*, 2009*b*). As an evolution of the bi-lens system and to expand the scope of its applications, we later introduced an interferometer consisting of six lens arrays (Snigirev *et al.*, 2014). The enlargement of the interferometer aperture leads to an increase of contrast of the interference pattern and to narrowing of the interference fringes. Compared with a bi-lens system, the six-lens interferometer forms an interference pattern with rich longitudinal structure, which can be described using the Talbot imaging formalism (Talbot, 1836).

In this paper, as a next step in the development of in-line interferometers, we present a multi-lens interferometer consisting of 30 parallel arrays of CRLs (so-called *triacanta*). The interferometer acceptance is comparable with the full size of the beam at the ESRF undulator beamline. The optical properties of the interferometer were studied using high photon energies in the range 32–65 keV at the 100 m-long ID11 ESRF beamline. The interference patterns generated by the interferometer were recorded at the first and second fractional Talbot distances. The effective source size was measured from the width of the interference fringes.

2. Interferometer description

A schematic view of the planar parabolic multi-lens interferometer is depicted in Fig. 1(*a*). The 30-lens interferometer is conceptually similar to the six-lens interferometer presented earlier (Snigirev *et al.*, 2014), except that it consists of 30 CRLs across the beam. Each CRL focuses the beam at a distance $z_f = F/[1 - (F/z_0)]$, where $F = (R/2)N\delta$ is the lens focal length, z_0 is the source-to-lens distance, R is the radius of curvature of one parabolic surface, N is the number of double concave elements in the CRL and δ is the decrement of complex refractive index n. Under coherent illumination, lenses generate diffraction-limited focal spots (secondary sources) of size $w_f = 0.44\lambda z_f/A_{eff}$, where λ is the wavelength and $A_{eff} = 0.66(\delta\lambda z_f/\beta)$ is the absorption-limited effective aperture of the lens (Kohn, 2012). At a distance $z > (z_f A_{int})/A_{eff}$ from the focal plane, where A_{int} is the physical aperture of the interferometer, the cones diverging from secondary sources overlap, and in this region interference occurs. The interference fringe pattern produced by the multi-lens interferometer can be described using the Talbot imaging formalism, with the only difference being that the classical amplitude grid used in Talbot imaging is replaced by a collection of periodic line secondary sources produced by the linear lens arrays and separated by a distance d. In the case of plane-wave illumination, the fundamental Talbot image appears at a distance $z_T = 2d^2/\lambda$ and fractional Talbot images are located at distances $z_n = z_T/2n$, where n is an integer. We note that the Talbot distance is measured from the lens foci, and that these foci are reproduced in the Talbot planes and are multiply reproduced in the fractional Talbot planes.

The interferometer was manufactured using electron-beam lithography and deep silicon etching called the BOSCH process (Snigirev *et al.*, 2007). A scanning electron microscope (SEM) image of the 30-lens interferometer is shown in

(*a*)

1 mm

(*b*)
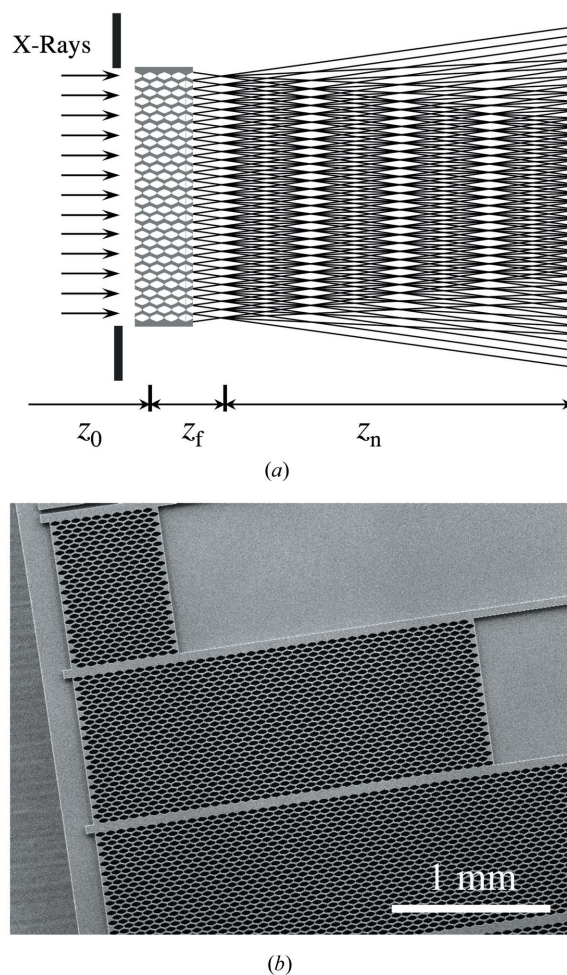
Figure 1
(*a*) Schematic view of the interferometer. (*b*) SEM image of the interferometer fabricated in the Si substrate.

Fig. 1(*b*). The longitudinal length and the physical aperture of the one elementary double concave lens are 62 and 30 μm, respectively. The radius at an apex of the parabolic surface R is 3.75 μm. The period d of the interferometer across the beam is equal to the physical aperture of one lens array, namely, $d = 30$ μm. The lens arrays in the interferometer are arranged in a chessboard pattern, similarly to the six-lens interferometer (Snigirev *et al.*, 2014). The beam acceptance of the *triacanta* interferometer is $A_i = 900$ μm (30 μm × 30 μm), which matches the beam size at 100 m downstream from the source at the undulator beamlines at the ESRF.

With the aim to expand the applicability of multi-lens interferometers for a wide range of energies, five *triacanta* sets were manufactured on the same Si chip. They were formally designed for the energy range from 10 to 50 keV with 10 keV steps. The focal distance of the interferometers for each energy was fixed at $F = 4$ cm, achieved by varying the number of individual double concave lenses in the CRL arrays of each interferometer. The selection of the proper interferometer set, which is suitable for the desired energy, can be performed by parallel displacement (across the beam) of the chip in the vertical direction. Table 1 summarizes the main parameters of the interferometer sets.

Table 1
Parameters of the 30-lens interferometer.

Set number	Energy (keV)	Number of lenses	Lens length (µm)	Diffraction-limited resolution (nm)†	Effective aperture (µm)
1	10	10	618	190	13
2	20	39	2416	87	17
3	30	87	5392	63	21
4	40	156	9670	55	23
5	50	243	15064	53	23

† Diffraction-limited resolution calculated for a single-lens array in the interferometer.

3. Experiment

Experimental tests of the 30-lens interferometer were performed at the long (about 100 m) ID11 ESRF beamline. Monochromatization of the incoming X-rays was performed by the double bent-crystal monochromator operating in a horizontal Laue geometry. Compared with flat crystals in Bragg geometry, asymmetrically cut bent crystals give up to 10× higher photon flux, notably at higher energies. The horizontal geometry allows direct cooling of the crystal by contact with a thermally controlled InGa bath. Attenuators located upstream from the monochromator removed essentially all flux below 25 keV; this, coupled with the Laue geometry, ensures very low thermal load compared with Bragg geometry monochromators. As a consequence, the monochromator is very stable, needing no adjustment or feedback after alignment. The horizontal geometry also minimizes the perturbation of the vertical source size. The vertical source size s was measured by direct imaging using CRLs (Weitkamp et al., 2001); during the 30-lens interferometer tests it was of the order of 15 µm.

During the experimental tests the *triacanta* was mounted on the stage with all necessary rotation and translation movements allowing the alignment in the beam at a distance $z_0 = 41.4$ m from the source. A sketch of the experimental scheme is presented in Fig. 1(a). Measurement of the interference patterns was performed using a high-resolution X-ray CCD camera equipped with a fluorescence screen and an optical objective which allows one to obtain 3 µm spatial resolution (effective pixel size of 1.5 µm). The quality of the fringes produced by the *triacanta* can be described quantitatively using a visibility parameter $V = \Delta I / I_a \times 100\%$, where $\Delta I = (I_{max} - I_{min})$ and $I_a = (I_{max} + I_{min})$. I_{max} and I_{min} are the irradiances corresponding to the maximum and the nearby minimum, respectively, in the fringe system.

Taking into account the specificity of ID11 as a long beamline specialized for the high energies, we studied the multi-lens interferometer optical properties with X-rays at energies of 32 and 65 keV recording the fundamental and fractional Talbot images at a distance of about 100 m from the source. Considering that the observation distance is comparable with the distance from the interferometer to the source, the curvature of the incident wavefront has to be taken into account.

Fractional Talbot images will be magnified by the factor C_m:

$$C_m = (z_f + z'_n + z_0)/(z_0 + z_f), \quad (1)$$

and will be located at a distance z'_n which is obtained from the equation (Cowley, 1995)

$$\frac{1}{z_f + z'_n} + \frac{1}{z_0} = \frac{1}{F + z_n}. \quad (2)$$

From the formula (2), it follows that for X-rays at 32 keV the fundamental $n = 1$ Talbot image is located at a distance $z'_1 = 53$ m. The interferometer set #3 consisting of 87 lenses designed for 30 keV was chosen for this experiment.

The observed interference pattern and the intensity variation obtained along a line through the centre of the pattern orthogonal to the fringes are shown in Fig. 2. The fringe spacing measured is $d' = 68$ µm, which corresponds to the theoretical estimate. The visibility of the interference fringes is 86% with respect to the background. The measured interference fringe FWHM w_e is 20 µm. As this Talbot image has a period equivalent to the object period it is possible to estimate the effective source size s directly from the width of the interference fringes on the base of the source size projection s' onto the detector plane estimated as $s' = sC_s$, where

$$C_s = (z_f + z'_n)/(z_0 + z_f). \quad (3)$$

If s' is much larger than the diffraction-limited width of the interference fringes $w'_t = w_t C_m$, where $w_t \simeq (0.92/M)\Lambda$, M is the number of CRL arrays in the interferometer and Λ is the fringe period for the plane illumination (Snigirev et al., 2014), then the source size can be directly estimated from the width of the experimental interference fringe w_e as $s = w_e/C_s$. Therefore, we can calculate the effective source size as $s = s' z_0/(z'_1 + z_f) = 15.6$ µm, in good agreement with the result obtained by means of CRL imaging of the source (15 µm FWHM). This result is slightly greater than value of 12 µm calculated from machine parameters during the experiment: vertical emittance 4 pm, beta function 2.8 m (Franchi et al., 2011).
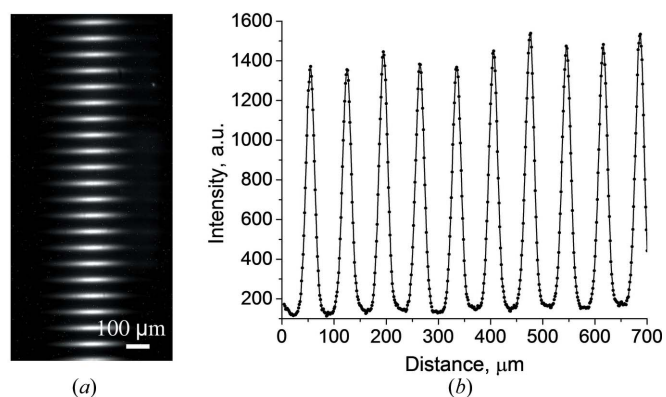
Figure 2
(a) Interference pattern generated by the *triacanta* recorded with X-rays at 32 keV. (b) Intensity variation obtained for the line through the centre of the fringe pattern; the contrast visibility is approximately 86%.
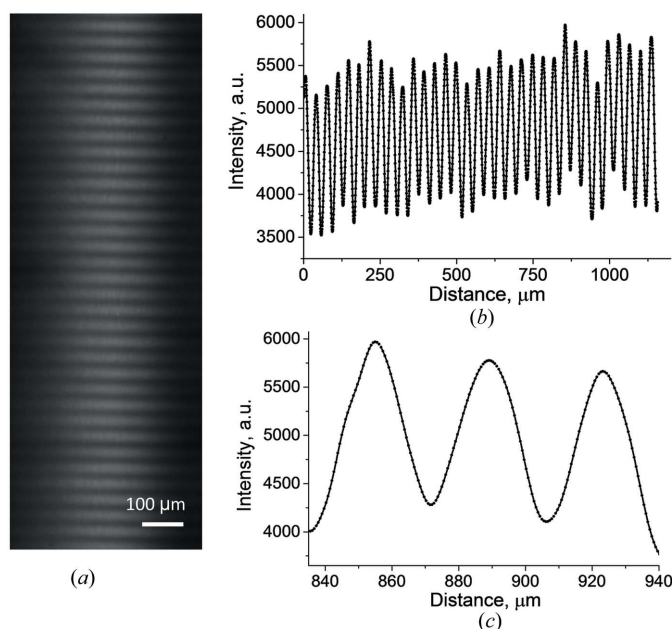
Figure 3
(a) Interference pattern generated at 65 keV. (b) Intensity variation obtained for the line through the centre of the fringe pattern. (c) Insert showing a visibility of approximately 17%.

Figure 4
Two-dimensional relative intensity distribution as a grey contrast map with the distance across a beam horizontally and the distance along a beam vertically. The black colour corresponds to zero intensity; the white colour corresponds to the maximum intensity.

We would like to point out that, for the measured source size, the spatial coherence length $L_{coh} = (\lambda s)/z_0$ at the interferometer position is of the order of 110 µm, from which it follows that less than four arrays were coherently illuminated. This proves the validity of our assumption that source size is dominant in the maxima width of the fringe pattern. In the case of almost diffraction-limited sources or full coherent illumination, it is necessary to convolute the source size projection with the diffraction-limited width of interference fringes.

In order to demonstrate the applicability of the interferometer at extremely high energies, we illuminated it with X-rays of 65 keV. For this we choose the interferometer set #5, which consists of 243 individual lenses giving the focal distance in the order of 7 cm. The fractional Talbot image with $n = 2$ which corresponds to $z'_2 = 53$ m was measured. The observed interference pattern together with the intensity variation obtained for the line through the centre of the fringe pattern is shown in Fig. 3. The registered fringe spacing of 36 µm is in agreement with calculations. The measured interference fringe visibility is 17%. The spatial coherence length L_{coh} at 65 keV is of the order of 60 µm, hence only the two nearest CRL arrays are illuminated coherently and only two beams can interfere. It follows from this that the *triacanta* works as a bi-lens interferometer and the interference fringe width w_e is equal to half of the period of the pattern, 18 µm. Therefore, it is impossible to estimate a source size directly from the interference pattern under these conditions.

4. Computer simulations

We have performed computer simulation for the interference pattern created by a 30-lens interferometer illuminated
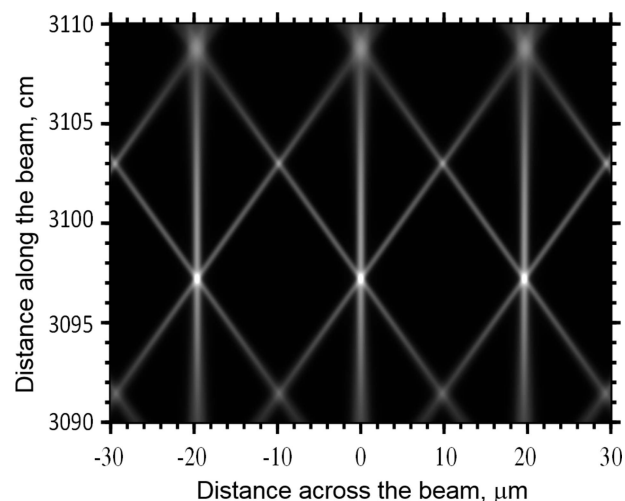
coherently at 65 keV. Consider a source size of 2 µm and the interferometer located at a distance of 100 m. In this case, the transverse coherent length $L_{coh} = 954$ µm is slightly greater than the interferometer aperture A_{int}. For computation of the interference patterns we used the algorithm described in our previous paper (Snigirev *et al.*, 2014). The calculations have been performed for interferometer set #5 composed of 243 lenses along the beam (the same system that has been used in the experiment; the focal distance is around 7 cm). We calculated interference patterns for z values varying from 30.9 m to 31.1 m with a 0.1 cm step near the second fractional Talbot image ($n = 2$, $z'_2 = 30.992$ m).

The calculated pattern representing the two-dimensional intensity distribution along the optical axis around the fractional $n = 2$ Talbot image is presented in Fig. 4. The calculations showed that the period of the fringes Λ is about 20 µm and fringe width w_e is 1.32 µm. It should be noted, however, that for a point source the fringe width is diffraction-limited and is $w_t \simeq (0.92/M)\Lambda \simeq 0.61$ µm. The source size projection to the detector plane in this case is $s' = 0.66$ µm, which is comparable with w_t. So this is the lower limit for using this interferometer for direct estimation of the source size because further reduction of the source size will not lead to narrowing of the interference fringe width.

As can be seen from Fig. 4, we found 'extra' fringes of a comparable intensity in addition to those expected. The main fringes are located at the same position across the optical axis (vertical lines) and only their intensity changes with the observation distance. At the same time, the additional fringes (inclined lines) change their position rather quickly. Fig. 5 shows cross sections of the two-dimensional intensity distribution across the optical axis, representing the movements of these additional fringes. At the position $z = 30.93$ m (Fig. 5a), two peaks are seen in addition to the main fringe reducing its intensity. At the position $z = 30.97$ m (Fig. 5b), the observed fringes have the maximum contrast and no additional peaks
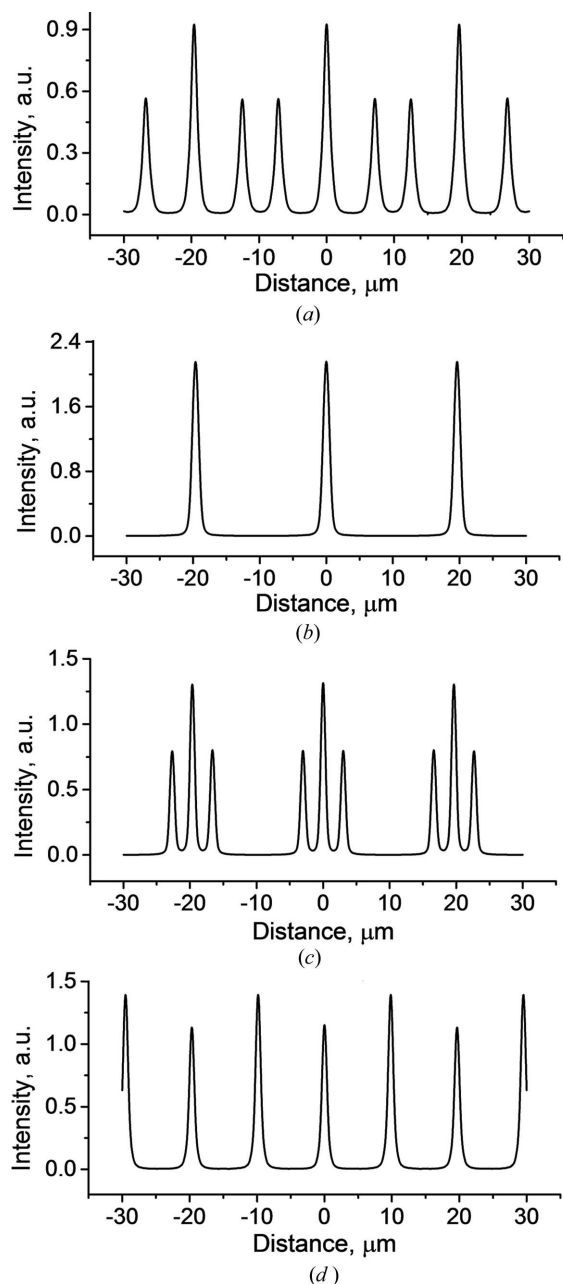
Figure 5
Computer simulations of interference fringes for various distances: (*a*) 30.93 m, (*b*) 30.97 m, (*c*) 30.99 m and (*d*) 31.03 m from the interferometer to the detector, respectively.

are observed. At the position z = 30.99 m (Fig. 5*c*), we have additional peaks close to the main ones. At the position z = 31.03 m (Fig. 5*d*), one can see additional peaks with the intensity comparable with the main fringes.

The reason for the appearance of additional fringes is the diffraction at the edges of the physical apertures of the CRLs. At such high energies, the effective aperture of the lens is larger than the physical one. In the case of Si as a lens material, the transmission at the lens borders is around 40%. Therefore, we have to consider that the lens acts as two gratings for Talbot imaging. In addition to the grating of focal lines produced by the linear lens arrays, we have to consider the

grating formed by the edges of the lenses' physical apertures. These gratings are spatially separated by a distance equal to the focal distance of the lens arrays. The coherent superposition of waves from these gratings in space leads to the appearance of 'extra' fringes in the interference pattern. To prove our concept that additional peaks are associated with the lens aperture edges, we calculated an interference pattern for the same experimental conditions, but taking a lens made of a material 10× more absorbing. Numerical simulations showed that all extra fringes disappeared.

This effect was impossible to observe during the experimental tests because of the significant influence of the source size which leads to a broadening of interference fringes. Nevertheless, this effect requires an additional separate study. Surprisingly, this effect may be used as an amplifier for the interference contrast. Indeed at the exact Talbot position (n = 2, z_2' = 30.992 m), the fringe intensity is around 1.2 whereas a maximum intensity of 2.15 is achieved by matching of the position of additional fringes and Talbot fringes. On the other hand, this effect may lead to the reduction of intensity of Talbot fringes: at the position z_2' = 30.93 m the intensity of the Talbot fringes drops to 0.92. It should be noted that all intensity fluctuations take place inside the depth of field of the Talbot image; in other words, the longitudinal size of amplified and impaired fringes is very small.

Finally, we note that at the border of the aperture of the current *triacanta* the transmission of the X-ray wave is about 40%. Therefore. it would be possible to eliminate this effect by using the CRL from the more absorbing material.

5. Conclusions

A 30-lens interferometer for hard X-rays was designed and manufactured. The physical aperture of the interferometer, and thus the beam acceptance, is comparable with the size of the vertical beam at an ESRF undulator beamline. The optical properties of the interferometer were studied by using high photon energies in the range from 32 to 65 keV. The interference patterns generated by the interferometer were recorded at the fundamental and at the second fractional Talbot imaging distances. An effective source size of the order of 15 µm was determined from the first Talbot image, in full agreement with the result obtained *via* direct imaging of the source using CRLs. This proves the concept that a multi-lens interferometer can be used as a high-resolution tool for beam diagnostics. The experimental test with 65 keV irradiation confirmed the possibility of using of new interferometer with X-rays of high energies, although the spatial coherence length was insufficient to obtain high interference fringe contrast; but taking into account the ESRF upgrade program we expect to obtain more coherent illumination of the 30-lens interferometer in the near future.

The computer simulations of the interference fringes for 65 keV photon energy and coherent illumination (source size 2 µm, distance to source 100 m) were carried out and showed the theoretical performance of the interferometer under these conditions. Additional structure in the interference pattern is

observed, caused by the diffraction of X-rays on the edges of the CRL apertures.

The proposed multi-lens interferometer can be used as a wavefront diagnostic device in the focusing mode similar to the Shack–Hartmann wavefront sensor (Mayo & Sexton, 2004). Moreover, the wavefront curvature may be determined from the Talbot image position (Malacara-Doblado, 1997). In addition, one cannot exclude applying multi-lens devices as beam-conditioning optics for special illumination, projection and beam smoothing at future diffraction-limited synchrotron radiation and FEL sources (Bonet *et al.*, 1994).

Acknowledgements

References

Aristov, V., Grigoriev, M., Kuznetsov, S., Shabelnikov, L., Yunkin, V., Weitkamp, T., Rau, C., Snigireva, I., Snigirev, A., Hoffmann, M. & Voges, E. (2000). *Appl. Phys. Lett.* **77**, 4058–4060.

Bonet, E., Andrés, P., Barreiro, J. C. & Pons, A. (1994). *Opt. Commun.* **106**, 39–44.

Bosak, A., Snigireva, I., Napolskii, K. S. & Snigirev, A. (2010). *Adv. Mater.* **22**, 3256–3259.

Cowley, J. M. (1995). *Diffraction Physics*, 3rd ed. Amsterdam: North-Holland.

Drakopoulos, M., Snigirev, A., Snigireva, I. & Schilling, J. (2005). *Appl. Phys. Lett.* **86**, 014102.

Drakopoulos, M., Zegenhagen, J., Snigirev, A., Snigireva, I., Hauser, M., Eberl, K., Aristov, V., Shabelnikov, L. & Yunkin, V. (2002). *Appl. Phys. Lett.* **81**, 2279.

Ershov, P., Kuznetsov, S., Snigireva, I., Yunkin, V., Goikhman, A. & Snigirev, A. (2013). *J. Appl. Cryst.* **46**, 1475–1480.

Franchi, A., Farvacque, L., Chavanne, J., Ewald, F., Nash, B., Scheidt, K. & Tomás, R. (2011). *Phys. Rev. ST Accel. Beams*, **14**, 034002.

Kohn, V. G. (2012). *J. Synchrotron Rad.* **19**, 84–92.

Lengeler, B., Schroer, C. G., Richwin, M., Tümmler, J., Drakopoulos, M., Snigirev, A. & Snigireva, I. (1999b). *Appl. Phys. Lett.* **74**, 3924–3926.

Lengeler, B., Schroer, C., Tümmler, J., Benner, B., Richwin, M., Snigirev, A., Snigireva, I. & Drakopoulos, M. (1999a). *J. Synchrotron Rad.* **6**, 1153–1167.

Malacara-Doblado, D. (1997). *Opt. Eng.* **36**, 2016–2024.

Mayo, S. C. & Sexton, B. (2004). *Opt. Lett.* **29**, 866–868.

Petukhov, A. V., Thijssen, J. H. J., 't Hart, D. C., Imhof, A., van Blaaderen, A., Dolbnya, I. P., Snigirev, A., Moussaïd, A. & Snigireva, I. (2006). *J. Appl. Cryst.* **39**, 137–144.

Polikarpov, M., Snigireva, I. & Snigirev, A. (2014). *J. Synchrotron Rad.* **21**, 484–487.

Schroer, C. G., Kuhlmann, M., Hunger, U. T., Günzler, T. F., Kurapova, O., Feste, S., Frehse, F., Lengeler, B., Drakopoulos, M., Somogyi, A., Simionovici, A. S., Snigirev, A., Snigireva, I., Schug, C. & Schröder, W. H. (2003). *Appl. Phys. Lett.* **82**, 1485–1487.

Snigirev, A., Kohn, V., Snigireva, I. & Lengeler, B. (1996). *Nature (London)*, **384**, 49–51.

Snigirev, A. & Snigireva, I. (2008). *C. R. Phys.* **9**, 507–516.

Snigirev, A., Snigireva, I., Grigoriev, M., Yunkin, V., Di Michiel, M., Kuznetsov, S. & Vaughan, G. (2007). *Proc. SPIE*, **6705**, 670506.

Snigirev, A., Snigireva, I., Grigoriev, M., Yunkin, V., Di Michiel, M., Vaughan, G., Kohn, V. & Kuznetsov, S. (2009a). *J. Phys. Conf. Ser.* **186**, 012072.

Snigirev, A., Snigireva, I., Kohn, V., Yunkin, V., Kuznetsov, S., Grigoriev, M. B., Roth, T., Vaughan, G. & Detlefs, C. (2009b). *Phys. Rev. Lett.* **103**, 064801.

Snigirev, A., Snigireva, I., Lyubomirskiy, M., Kohn, V., Yunkin, V. & Kuznetsov, S. (2014). *Opt. Express*, **22**, 25842–25852.

Talbot, H. F. (1836). *Philos. Mag.* **3**, 401–407.

Vaughan, G. B. M., Wright, J. P., Bytchkov, A., Rossat, M., Gleyzolle, H., Snigireva, I. & Snigirev, A. (2011). *J. Synchrotron Rad.* **18**, 125–133.

Weitkamp, T., Chubar, O., Drakopoulos, M., Souvorov, A., Snigireva, I., Snigirev, A., Günzler, F., Schroer, C. & Lengeler, B. (2001). *Nucl. Instrum. Methods Phys. Res. A*, **467–468**, 248–251.